Cabrera, A.; Weinberg, R.; Wrigth, H.; Zlotnik, S. and Cas, R., Melt fracturing and healing: a mechanism for rhyolite magma degassing and origin of obsidian, *Geology*, Vol. 39, pp. 67-70, 2011

Melt fracturing and healing: a mechanism for degassing and origin of silicic obsidian

Agustín Cabrera, Roberto F. Weinberg, Heather M.N. Wright[*], Sergio Zlotnik[1], and Ray A.F. Cas

School of Geosciences and School of Mathematical Sciences[1], Building 28, Monash University, Clayton, VIC 3800, Australia

[*] *Currently at: U.S. Geological Survey, 345 Middlefield Rd, MS 910, Menlo Park, CA 94025 USA*

ABSTRACT

We present water content transects across a healed fault in pyroclastic obsidian from Lami pumice cone, Lipari, Italy, using synchrotron Fourier transform infrared spectroscopy. Results indicate that rhyolite melt degassed through the fault surface. Transects define a trough of low water content coincident with the fault trace, surrounded on either side by high water content plateaux. Plateaux indicate that obsidian on either side of the fault equilibrated at different *P-T* conditions before being juxtaposed. The curves into the troughs indicate disequilibrium and water loss through diffusion. If we assume constant *T*, melt equilibrated at pressures differing by 0.74 MPa before juxtaposition, and the fault acted as a low-pressure permeable path for H_2O that diffused from the glass within time scales of 10 and 30 min. Assuming constant *P* instead, melt on either side could have equilibrated at temperatures differing by up to 100 °C, before being brought together. Water content on the fault trace is particularly sensitive to post-healing diffusion. Its preserved value indicates either higher temperature or lower pressure than the surroundings, indicative of shear heating and dynamic

decompression. Our results reveal that water contents of obsidian on either side of the faults equilibrated under different *P-T* conditions and were out of equilibrium with each other when they were juxtaposed due to faulting immediately before the system was quenched. Degassing due to faulting could be linked to cyclical seismic and general degassing during silicic volcanic activity, and could be an efficient mechanism of producing low-water content obsidian.

INTRODUCTION

Obsidian is typically a vesicle- and crystal-poor glassy silicic volcanic rock (e.g., Dellino and Volpe, 1995). Pyroclastic obsidian generally has relatively high water contents, (~0.5 and ~1.5 wt%; e.g., Castro and Dingwell, 2009; Eichelberger and Westrich, 1981; Rust and Cashman, 2007), when compared to similar lavas (~0.3 and 0.1 wt%; e.g., Eichelberger et al., 1986; Friedman, 1989). Generation of relatively degassed but poorly vesicular obsidian is poorly understood and is ascribed to gas loss either through vesicles (e.g., Eichelberger et al., 1986; Okumura et al., 2009) or along fractures in magma (Gonnermann and Manga, 2003; 2005; 2007; Rust and Cashman, 2007; Rust et al., 2004; Stasiuk et al., 1996). Details of this mechanism remain poorly understood but volatile concentration measurements support models of degassing through fracturing (Rust et al. 2007; Tuffen et al. 2010).

Small-scale faults and welded breccias have recently been described in obsidian conduits, lavas and pyroclastic blocks (Gonnermann and Manga, 2003, 2005; Goto, 1999; Rust and Cashman, 2007; Rust et al., 2004; Tuffen et al., 2003; Tuffen and Dingwell, 2005). Evidence suggest a process of repeated fracturing and healing of melt (RFH) (Tuffen et al.; 2003; Tuffen and Dingwell, 2005) that may be characteristic of rhyolitic eruptions, as supported by numerical models (Gonnermann and Manga, 2003).

Here, we investigate rhyolite melt degassing through fractures. We carried out synchrotron Fourier transform infrared spectroscopy (SFTIR) transects at high angle to a rehealed fault in a juvenile obsidian pyroclastic bomb from the Lami pumice cone on Lipari, Italy. Water content profiles suggest degassing through fractures with significant implications for obsidian formation and conduit degassing.

SAMPLE DESCRIPTION AND METHODS

We report results from a healed fault in the glassy rind of one breadcrusted pyroclastic obsidian sample (LO1) from the Lami cone (Fig. 1), on the flank of the Mt Pilato pumice cone. These are part of the rhyolitic, explosive and effusive, Mt Pilato-Rocche Rosse sequence (e.g., Cortese et al., 1986; Dellino and Volpe, 1995). The wall of the Lami cone reveals ~1 m thick obsidian-rich layers interlayered with white tube pumice-rich layers (Fig. 1C) interpreted as fallout coeval to the eruption of the Mt Pilato pumice cone (Cortese et al., 1986). Clasts in obsidian-rich layers have similar chemistry to pumice counterparts and later obsidian lava (Table A1, in the GSA Data Repository1). Obsidian-rich layers are exclusively formed by breadcrusted clasts, lapilli to bomb size, and lapilli size obsidian clasts similar to Pele's tears. Breadcrusted obsidian bombs have >1 cm thick black glassy rinds and foamed interiors that indicate post-fragmentation expansion, and form sag structures in underlying layers, suggesting ballistic emplacement (Fig. 1C and D).

The glassy rind of sample LO1 preserves a healed fault plane truncating folded microlite-rich bands and pristine glassy bands (Fig. 2). Fault is used to describe a fracture plane that accommodated movement. Microlites are thin, >20μm long needles comprising at most ~1 vol %. Some fold hinges have relatively undeformed vesicles. The healed fault is >3 cm long in a block ~10 cm across (Fig. 1D) which lacks evidence for brecciation. SFTIR transects were

carried out in two doubly polished wafers nearly perpendicular to the fault trace. (Figs. 2A and B) which is at right angle to wafer surface (except for transect B2 where the fault plane dips ~83° into wafer, measured using an optical microscope). Wafer thickness varied between 900 and 1000 µm, measured with a micrometer with precision of ± 5 µm. We report water concentrations along three transects (Figs. 2 and 3A) using a 10 µm diameter infra-red beam at intervals of 40 µm (for transects A1 and B1) and 60 µm (for transect B2). For each transect, points were analyzed along two parallel lines 80 to 100 µm apart. Water concentrations are reported as a single traverse, using the average of the two adjacent analyses (Fig. 3A). These were used to compute uncertainty (gray bands in profiles in Fig. 3A), which is <3% of measured values. Errors associated with thickness measurements or microlite influence are smaller than variations from repeated measurements along the two parallel transect. We used 128 scans for each spectrum and analyzed background after every 10 measurements. Total H_2O concentrations were determined from the intensity of the broad 4500 cm^{-1} and 5200 cm^{-1} absorption bands, and total water concentration (H_2O_{total}) was calculated according to Zhang et al. (1997). Peak heights were ~3 times greater for the OH^- peak (4500 cm^{-1}) than the H_2O peak (5200 cm^{-1}). Carbon dioxide concentration was below detection.

RESULTS

Synchrotron FTIR Water Profiles

SFTIR transects define two plateaux of nearly constant water content separated by a V-shaped trough coincident with the fault trace (Fig. 3A). Water content for transect A1 decreases rapidly from the plateaux toward the trough over a region ~480 µm wide. The difference in water content between the plateaux on the left (0.66 wt% H_2O) and the right (0.73 wt% H_2O) is ~0.07

wt%, and up to 0.12 wt% higher than the trough (0.61 wt% H_2O). The slope from plateau to trough is steeper and sharper on the right than on the left. Similarly, the V-shaped trough in B2 is ~480 μm wide, but the plateau on left (0.76 wt%) and right (0.78 wt%) sides have closer values, up to ~0.10 wt% higher than the trough (0.68 wt%). In contrast, water content along the third transect, B1, does not define a plateau and water decreases continuously over ~600 μm.

DISCUSSION

The volatile content of a given melt is controlled by temperature and pressure. Previous studies of degassing have focused on decompression (Gonnermann and Manga, 2007), here we also consider temperature variation.

Troughs and Water Diffusion Profiles

Water content curves are fitted by diffusion profiles (Fig. 3B). Here we quantify diffusion into the fault (Fig. 2) following Castro et al. (2005, 2008). We consider that water diffusion began upon fracturing and ceased upon healing. This assumes negligible time for post-healing diffusion, implying rapid quenching (Fig. 3B), as supported by preservation of delicate water diffusion curves (above). Water diffusivity in silicate melt has Arrhenian dependence on *T*, negligible dependence on *P*, and is a function of H_2O content (*C*) (Ni and Zhang, 2008). We solved numerically the 1*D* diffusion equation:

$$\frac{\partial C}{\partial t} = \frac{\partial}{\partial x}\left[D(C,T,P)\frac{\partial C}{\partial x} \right], \quad (1)$$

where *D(C, T, P)* is the diffusivity of H_2O in rhyolite melt (Ni and Zhang, 2008). We assumed either: a) constant *T* everywhere and determined the best diffusion time (Fig. 3B), or b) similar time for diffusion on both sides of the fault, and calculated *T* (Fig. 4).

For constant *T* models, calculations were carried out at 50 °C intervals between 750 and 950 °C. The initial water content for each diffusion profile is set to the average of each plateau

(Fig. 3B). The fault trace has the lowest water content in the profile and water flux in the plateau boundary of the model is defined as $\partial C / \partial x = 0$. The best fit model is the one that minimizes mean absolute error. For variations in measured water contents, uncertainties for modeled diffusion times vary between 20 and 35% of reported values. Multiple fractures (Fig. 2B) could explain the lack of plateaux in transect B1 (Fig. 3A). Diffusion times or equilibrium conditions cannot be determined for B1 so we do not report on it any further.

For constant *T*, calculated diffusion times vary from 73.7 min at 750 °C to 3.9 min at 950 °C (Fig. 4). For an eruptive temperature of 850 °C (Davì et al., 2009), diffusion lasted between 10 and 30 min for the different curves. Longer diffusion times can be reached for unreasonably low temperatures (Fig. 4). There is an issue, however, with results assuming constant *T*: they yield different best-fit diffusion times for each side of the fault across the same profile (Fig. 3B). This requires melt on each side to be exposed to diffusion into the fault for different time spans, which we deem unlikely.

Our second approach was to equate diffusion time on either side of the fault and assume that *T*, and therefore *D*, varied. Figure 4 and Table 1 show that to attain equal diffusion times, temperature differences across the fault would have been 80–100 °C for A1, and 30–40 °C for B2. Furthermore, Figure 4 indicates that melts at 750 and 830 °C on either side of the fault in A1 would produce the diffusion curves over a time span of 30 min. These temperatures are close to those estimated independently for equilibration of the plateaux water contents (see next section). The higher value of thermal diffusivity compared to water diffusivity implies that thermal equilibrium would be reached before significant water diffusion. Thus, if water diffusion take place at different temperatures, it would have taken place before the two melt portions were juxtaposed by the fault.

Calculations of the evolution of water content on a fault plane with initially 0% water, surrounded by two high water content plateaux on either side, reveal that post-healing diffusion raises water content on the fault to the measured value of 0.6% in less than 60s. This indicates the sensitivity of the trough and that post-healing diffusion longer than 60s would have given rise to a shallower, U-shaped trough. Thus, post-healing diffusion implies that water content on the fault would have been lower at healing, and that *P-T* estimates for the fault itself are conservative: lower *P* and higher *T* could have prevailed before healing.

Plateaux Indicative of Early Equilibrium

Plateaux pairs in A1 and B2 indicate that water content in the small volumes of melt on either side of the fault had at some point reached equilibrium with surrounding *P-T* conditions. However, in A1 (Fig. 3) the plateau on the left (0.66 wt% H_2O) contains less water than the one on the right (0.73 wt% H_2O). Because the two sides are in contact, they could not both have been in equilibrium with surrounding *P-T* simultaneously. We therefore infer that fault displacement brought them into contact after they equilibrated in regions with different *P-T* conditions. Thus, water contents in melts across the fault were both out of equilibrium with conditions imposed by the fault and out of equilibrium with the surroundings after faulting.

Assuming that the small portion of melts were at identical and constant *T* before faulting, we estimate the difference in equilibration pressure (ΔP), by translating the average water content of each plateaux to pressures, using established relationships (Newman and Lowenstern 2002). Considering magmatic pressure (i.e., no overpressure), ΔP is further translated to depth difference (ΔZ). For rhyolite density of 2323 kg/m^3 (calculated for Lami composition with ~0.7 wt % H_2O, at ~3.8MPa and *T* between of 750-950 ^oC; Spera, 2000) and *T* = 850 °C, the water difference between the plateaux in A1 of ~0.07 wt% corresponds to a ΔP of 0.74 MPa, for CO_2 =

0 ppm (Newman and Lowenstern, 2002) and a ΔZ of ~32 m. These are maximum values since melts could have been overpressurized or at different temperatures. Using estimated ΔP, ΔZ and diffusion times, we estimate relative melt decompression rate and relative vertical velocity across the fault (the word "relative" refers to one side in relation to the other, not absolute values). Typical times between 10 and 30 min yield a relative decompression rate between 1.5 and 4.5 MPa h^{-1} and a relative vertical velocity between 1.8 and 4.8 cm sec^{-1}.

Alternatively, assuming constant *P*, we investigate whether *T* variations explains water variations. For *P* = 3.8 MPa (Newman and Lowenstern, 2002), the plateaux pair in A1 at 0.66 wt% H_2O and 0.73 wt% H_2O would have been in equilibrium if *T* was ~850 °C and 750 °C, respectively. For these values, diffusion curves on either side of the fault would both be resolved for an identical diffusion time of 30 min (Table 1). This is unlike the case where we varied *P*, for which each side had a different diffusion time. Furthermore, for *P* = 3.8 MPa even within the fault plane, the 0.61 wt% H_2O in the trough would have been in equilibrium for *T* = 950 °C (Newman and Lowenstern, 2002). This suggests that shear heating on the fault (Hess et al., 2008) could explain the origin of the trough, and like for pseudotachylites, the total amount of energy due to shearing is sufficient only to raise temperatures within a narrow band.

Our simple approach assumes fixed water content in the deep part of the trough, and that water diffuses toward this value. Our two end-member cases indicate that the trough in A1 could represent either the minimum *P* site (in equilibrium at 3.2 MPa for *T* = 850 °C), or the maximum *T* site (in equilibrium at 950 °C for *P* = 3.8 MPa). In summary, SFTIR results indicate water disequilibrium at two levels: a) parcels of magmas had reached equilibrium, as indicated by plateaux, but faulting displaced them to new conditions. Melt on either side of the fault either equilibrated ~30 m apart vertically (for constant *T*), or had ~100 °C temperature difference (for

constant *P*). They were then brought together by faulting and were no longer in equilibrium. b) The fault plane imposed new, dynamic *P-T* conditions and a permeable path for volatiles, giving rise to diffusion profiles which indicate active faulting and healing for 10–30 min. Solutions of diffusion curve pairs for similar times require temperature differences of ~100 °C, similar to that estimated for pre-faulting plateaux equilibration at constant *P*. The loss of volatiles from the melt through diffusion inhibits vesiculation. Temperature increases due to shear heating eases vesiculation but also favors volatile loss into faults due to increased diffusivity.

Autobrecciation and Melt Degassing: Obsidian Formation

Non-explosive fragmentation of ascending magmas has been inferred based on clastic textures (Tuffen et al., 2003), supported by earthquakes during dome-forming silicic eruptions (Goto, 1999), and modeled for magma ascent in conduits (Cordonnier et al., 2009; Gonnermann and Manga, 2003). We have shown that degassing occurs through fracturing in rhyolitic melts, supporting suggestions that repeated fracturing and healing (RFH) assists degassing, suppressing vesiculation and favoring obsidian formation (Gonnermann and Manga, 2005; Rust and Cashman, 2007; Rust et al., 2004; Tuffen et al. 2010).

If this is so, fracturing and degassing should proceed at rates compatible with magma movement in the conduit. We note that faulting and healing duration, here constrained to 10^2-10^3 s, are less than but broadly comparable with estimates of the timescale for RFH from a simple fracture and welding model (Tuffen et al. 2003), and compatible with inter-event time for hybrid and long-period earthquake events during dome eruptions ($10^{2.5}$-$10^{4\,5}$ seconds; Voight et al., 1999), possibly linked to RFH (Tuffen et al., 2003). We postulate that degassing due to RFH events in conduits could explain the temporal shift from explosive to effusive eruption common

in silicic systems (Castro and Dingwell, 2009; Eichelberger et al., 1986; Fink, 1983), including those in Lipari.

CONCLUSIONS

Results show that water diffused from the melt into a low *P* or high *T* fault plane. Water diffusion into the fault lasted between ~10 and 30 min before healing and quenching. Different water plateaux determined for melts on either side of the fault indicates that each side had achieved equilibrium in terms of water content before being brought together by faulting into new *P-T* conditions. The duration of the process match roughly that of the repeat time of earthquakes during silicic lava eruptions (Tuffen et al., 2003). Results indicate that pervasive fracturing is a potential mechanism for degassing of rhyolite magma, explaining the origin of obsidian and the commonly observed temporal shift from explosive to effusive eruptions.

AKNOWLEDGMENTS

Laboratory work was undertaken at the Australian Synchrotron. We thank Y. Zhang for helping on water diffusivity calculations and J. Castro for constructive comments. We appreciated the comments from H. Tuffen, L Caricchi and an anonymous reviewer that greatly improved this manuscript.

REFERENCES CITED

Castro, J.M., Manga, M., and Martin, M.C., 2005, Vesiculation rates of obsidian domes inferred from H2O concentration profiles (DOI 10.1029/2005GL024029): Geophysical research letters, v. 32, p. 21307.

Castro, J.M., Beck, P., Tuffen, H., Nichols, A.R.L., Dingwell, D.B., and Martin, M.C., 2008, Timescales of spherulite crystallization in obsidian inferred from water concentration profiles: American Mineralogist, v. 93, p. 1816-1822.

Castro, J.M., and Dingwell, D.B., 2009, Rapid ascent of rhyolitic magma at Chaiten volcano, Chile: Nature, v. 461, p. 780–783, doi:10.1038/nature08458.

Cordonnier, B., Hess, K.U., Lavallée, Y., and Dingwell, D.B., 2009, Rheological properties of dome lavas: Case study of Unzen volcano: Earth and Planetary Science Letters, v. 279, p. 263–272, doi:10.1016/j.epsl.2009.01.014.

Cortese, M., Frazzetta, G., and Lavolpe, L., 1986, Volcanic history of Lipari (Aeolian Islands, Italy) during the last 10,000 years: Journal of Volcanology and Geothermal Research, v. 27, p. 117–133, doi:10.1016/0377-0273(86)90082-X.

Davì, M., Behrens, H., Vetere, F., and De Rosa, R., 2009, The viscosity of latitic melts from Lipari (Aeolian Islands, Italy): Inference on mixing-mingling processes in magmas: Chemical Geology, v. 259, p. 89–97, doi:10.1016/j.chemgeo.2008.10.009.

Dellino, P., and Volpe, L.L., 1995, Fragmentation versus transportation mechanisms in the pyroclastic sequence of Monte Pilato-Rocche Rosse (Lipari, Italy): Journal of Volcanology and Geothermal Research, v. 64, p. 211–231, doi:10.1016/0377-0273(94)00084-T.

Eichelberger, J.C., and Westrich, H.R., 1981, Magmatic volatiles in explosive rhyolitic eruptions: Geophysical Research Letters, v. 8, p. 757–760, doi:10.1029/GL008i007p00757.

Eichelberger, J.C., Carrigan, C.R., Westrich, H.R., and Price, R.H., 1986, Non-explosive silicic volcanism: Nature, v. 323, p. 598–602, doi:10.1038/323598a0.

Fink, J.H., 1983, Structure and emplacement of a rhyolitic obsidian flow. Little Glass Mountain, Medicine Lake highland, northern California: Geological Society of America Bulletin, v. 94, p. 362–380, doi:10.1130/0016-7606(1983)94<362:SAEOAR>2.0.CO;2.

Friedman, I., 1989, Are extrusive rhyolites produced from permeable foam eruptions?: Bulletin of Volcanology, v. 51, p. 69–71, doi:10.1007/BF01086762.

Gonnermann, H.M., and Manga, M., 2003, Explosive volcanism may not be an inevitable consequence of magma fragmentation: Nature, v. 426, p. 432–435, doi:10.1038/nature02138.

Gonnermann, H.M., and Manga, M., 2005, Nonequilibrium magma degassing: results from modeling of the ca. 1340 A.D. eruption of Mono Craters, California: Earth and Planetary Science Letters, v. 238, p. 1–16, doi:10.1016/j.epsl.2005.07.021.

Gonnermann, H.M., and Manga, M., 2007, The fluid mechanics inside a volcano: Annual Review of Fluid Mechanics, v. 39, p. 321–356, doi:10.1146/annurev.fluid.39.050905.110207.

Goto, A., 1999, A new model for volcanic earthquake at Unzen Volcano: Melt rupture model: Geophysical Research Letters, v. 26, p. 2541–2544, doi:10.1029/1999GL900569.

Hess, K.-U., Cordonnier, B., Lavallée, Y., and Dingwell, D.B., 2008, Viscous heating in rhyolite: An in situ experimental determination: Earth and Planetary Science Letters, v. 275, p. 121–126, doi:10.1016/j.epsl.2008.08.014.

Newman, S., and Lowenstern, J.B., 2002, VC: a silicate melt-H2O–CO2 solution model written in Visual Basic for excel: Computers & Geosciences, v. 28, p. 597–604, doi:10.1016/S0098-3004(01)00081-4.

Ni, H., and Zhang, Y., 2008, H2O diffusion models in rhyolitic melt with new high pressure data: Chemical Geology, v. 250, p. 68–78, doi:10.1016/j.chemgeo.2008.02.011.

Okumura, S., Nakamura, M., Takeuchi, S., Tsuchiyama, A., Nakano, T., and Uesugi, K., 2009, Magma deformation may induce non-explosive volcanism via degassing through bubble networks: Earth and Planetary Science Letters, v. 281, p. 267–274, doi:10.1016/j.epsl.2009.02.036.

Rust, A., and Cashman, K., 2007, Multiple origins of obsidian pyroclasts and implications for changes in the dynamics of the 1300 B.P. eruption of Newberry Volcano, USA: Bulletin of Volcanology, v. 69, p. 825–845, doi:10.1007/s00445-006-0111-4.

Rust, A.C., Cashman, K.V., and Wallace, P.J., 2004, Magma degassing buffered by vapor flow through brecciated conduit margins: Geology, v. 32, p. 349–352, doi:10.1130/G20388.2.

Spera, F.J., 2000, Physical properties of magmas, In: Sigurdsson H, Houghton BF, McNutt SR, Rymer H, Stix J (eds) Encyclopedia of volcanoes. Academic Press, San Diego, pp 171–190.

Stasiuk, M.V., Barclay, J., Carroll, M.R., Jaupart, C., Ratté, J.C., Sparks, R.S.J., and Tait, S.R., 1996, Degassing during magma ascent in the Mule Creek vent (USA): Bulletin of Volcanology, v. 58, p. 117–130, doi:10.1007/s004450050130.

Tuffen, H., Dingwell, D.B., and Pinkerton, H., 2003, Repeated fracture and healing of silicic magma generate flow banding and earthquakes?: Geology, v. 31, p. 1089–1092, doi:10.1130/G19777.1.

Tuffen, H., and Dingwell, D., 2005, Fault textures in volcanic conduits: evidence for seismic trigger mechanisms during silicic eruptions: Bulletin of Volcanology, v. 67, p. 370–387, doi:10.1007/s00445-004-0383-5.

Tuffen, H., Owen, J., and Denton, J., 2010, Magma degassing during subglacial eruptions and its use to reconstruct palaeo-ice thicknesses: Earth-science reviews, v. 99, p. 1-18.

Voight, B., Sparks, R.S., nbsp, J, Miller, A.D., Stewart, R.C., Hoblitt, R.P., Clarke, A., Ewart, J., Aspinall, W.P., Baptie, B., Calder, E.S., Cole, P., Druitt, T.H., Hartford, C., Herd, R.A., Jackson, P., Lejeune, A.M., Lockhart, A.B., Loughlin, S.C., Luckett, R., Lynch, L., Norton, G.E., Robertson, R., Watson, I.M., Watts, R., and Young, S.R., 1999, Magma flow

instability and cyclic activity at Soufriere Hills volcano, Montserrat, British West Indies: Science, v. 283, p. 1138–1142.

Zhang, Y., Belcher, R., Ihinger, P.D., Wang, L., Xu, Z., and Newman, S., 1997, New calibration of infrared measurement of dissolved water in rhyolitic glasses: Geochimica et Cosmochimica Acta, v. 61, p. 3089–3100, doi:10.1016/S0016-7037(97)00151-8.

FIGURE CAPTIONS

Figure 1. Location of Aeolian Islands and Lipari, southern Italy. B. Sketch of Lipari Island highlighting location of Mt Pilato-RR sequence (line pattern) and Lami cone (star) in north-east; black arrow points to Lami cone. C. Overview of exposure of Lami deposits showing dark layers of obsidian interlayered with white pumice layers. Circle highlights a sag structure and location of sample LO1. D. Photograph of fragment of sample LO1 with black, outer breadcrusted obsidian rind at base and white pumiceous interior at top.

Figure 2. A–B. Photomicrographs of wafers A and B, respectively. Double lines mark the position of the three SFTIR transects (A1, B2 and B1) across fault truncating flow banding. Line drawings illustrates flow folding patterns, dashed lines mark fault traces. C–D. Enlargement of B showing transects B2 and B1. Cloudy bands on glass are microlite-rich of similar mineralogy everywhere (>20 μm long needles of pyroxene), dark ellipses at fold hinges are vesicles.

Figure 3. A. Synchrotron FTIR water content profiles for transects A1, B2 and B1. Grey bands are average lateral variations in measurements and represent uncertainties. B. Measurements and water diffusion profiles for different diffusion timescales. A1-L and A1-R are left- and right-hand-side synchrotron profiles in A1, respectively; likewise B2-L and B2-R are left and right-hand-side profiles in B2. Dashed lines represent position of fault trace.

Figure 4. Diffusion times for T between 750° – 950 °C. Best fit diffusion times for left- and right-hand-sides of sample A1 (A1-L and A1-R) and B2 (B2-L and B2-R, respectively). Dashed lines mark different T for each profile for similar diffusion time. Timescales longer than ~30 min and shorter than ~10 min require temperatures beyond modeled.

TABLE 1 Δ T FOR F XED T MES

A1 Time (min)	ΔT C°	**B2** Time (min)	ΔT C°
11	101	6	41
15	96	10	37 5
20	90	15	34 5
25	86	20	32
30	83	25	31

Note: Temperature variations (ΔT) on each side of the fault in A1 and B2 assuming diffusion curve pairs had equal times to develop

Cabrera Agustin, Figure 1. jpg

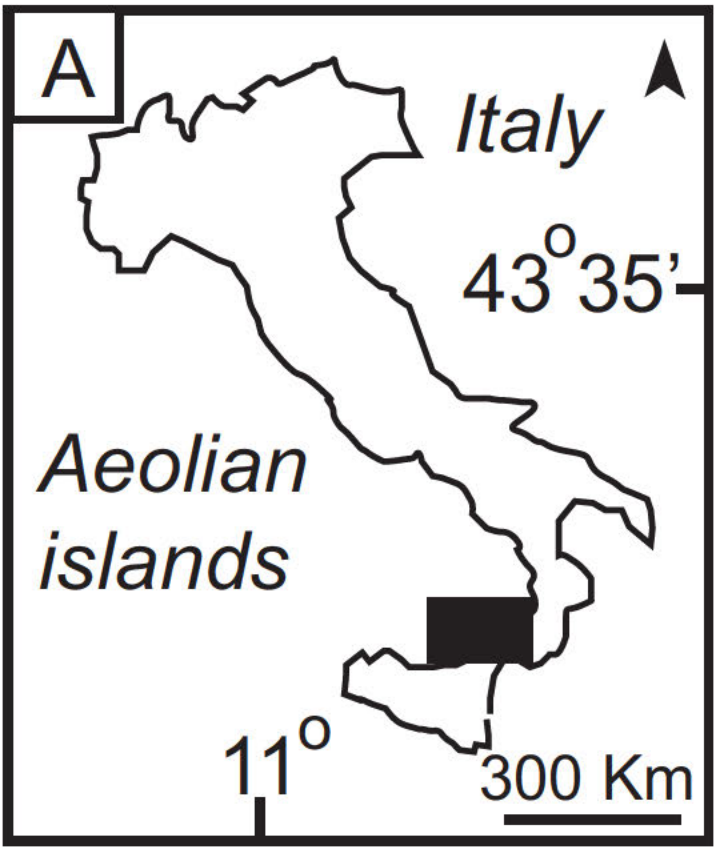

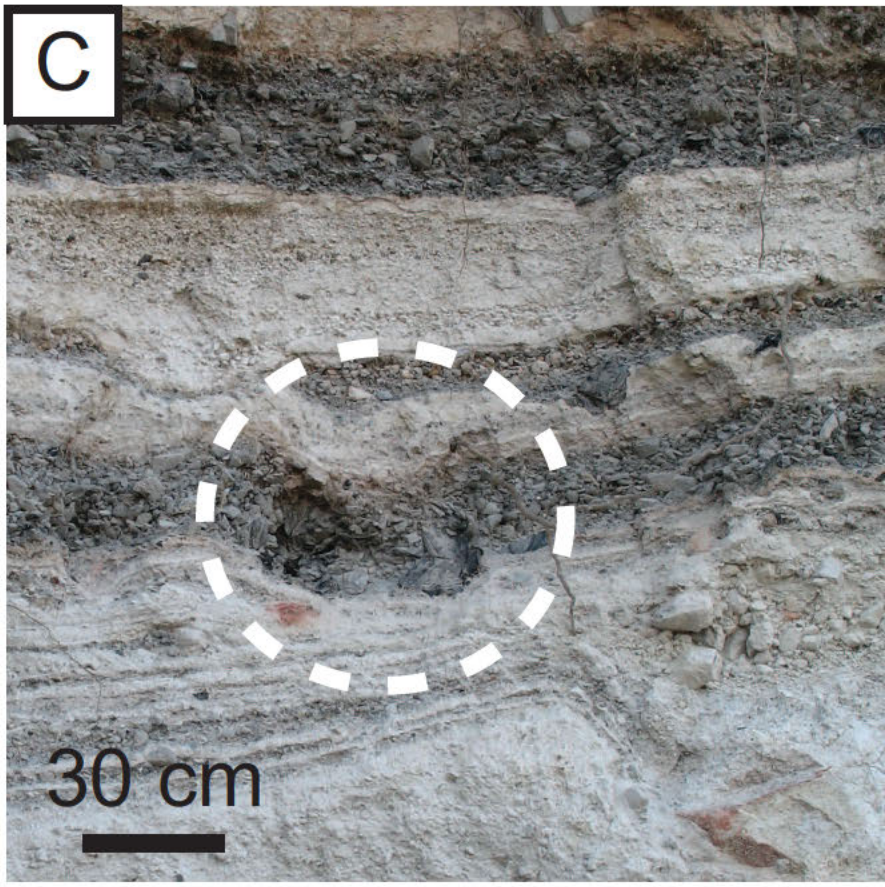

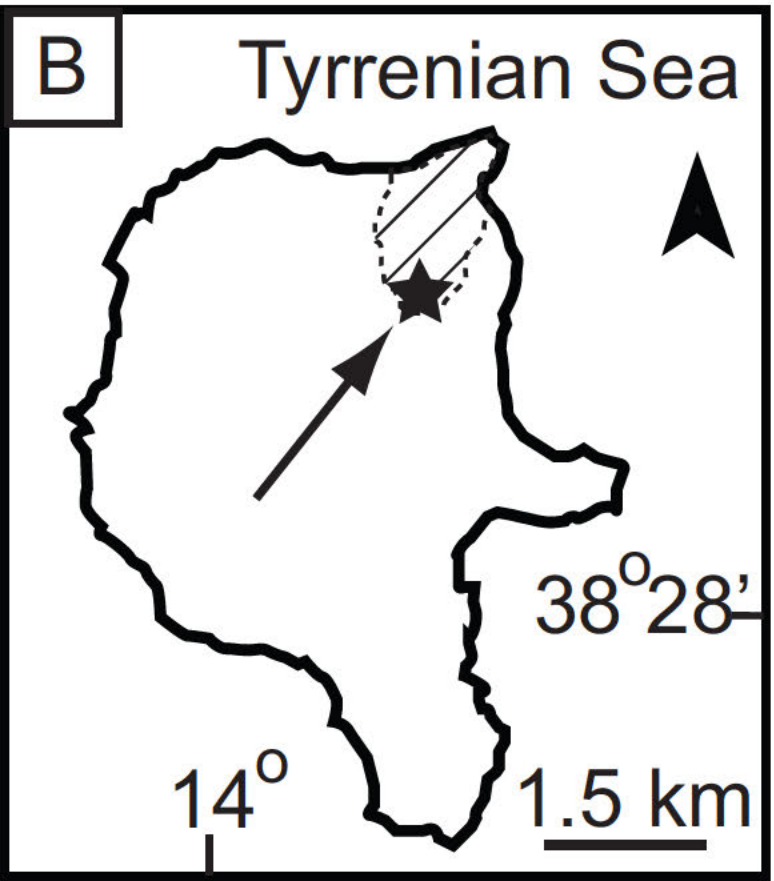

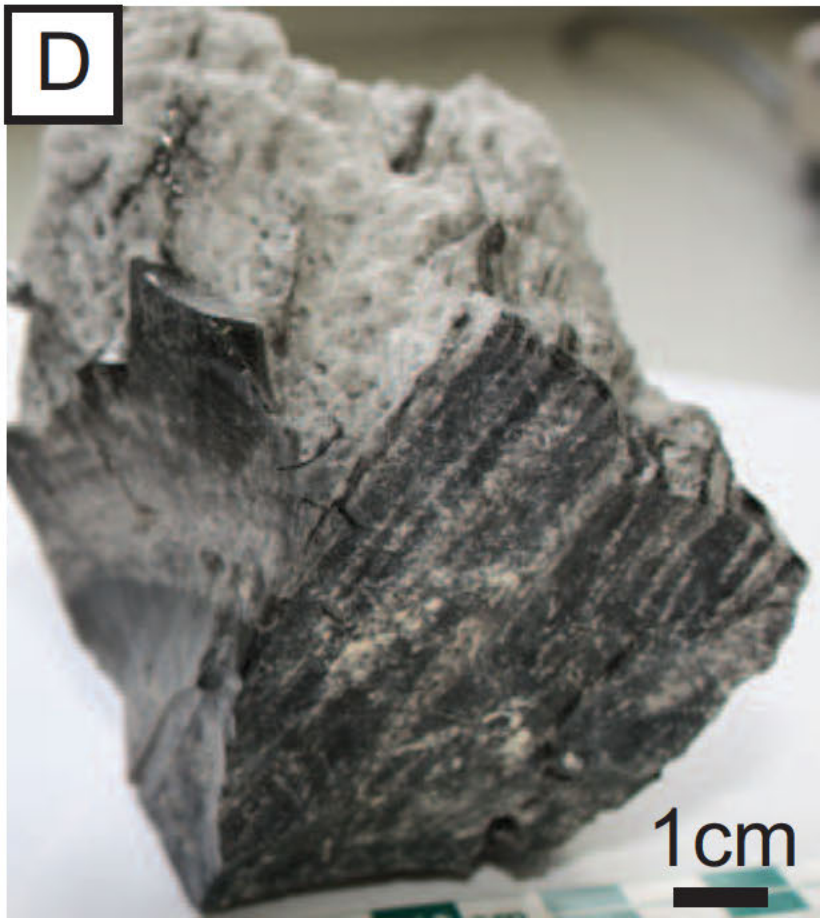

Cabrera Agustin, Figure 1. jpg

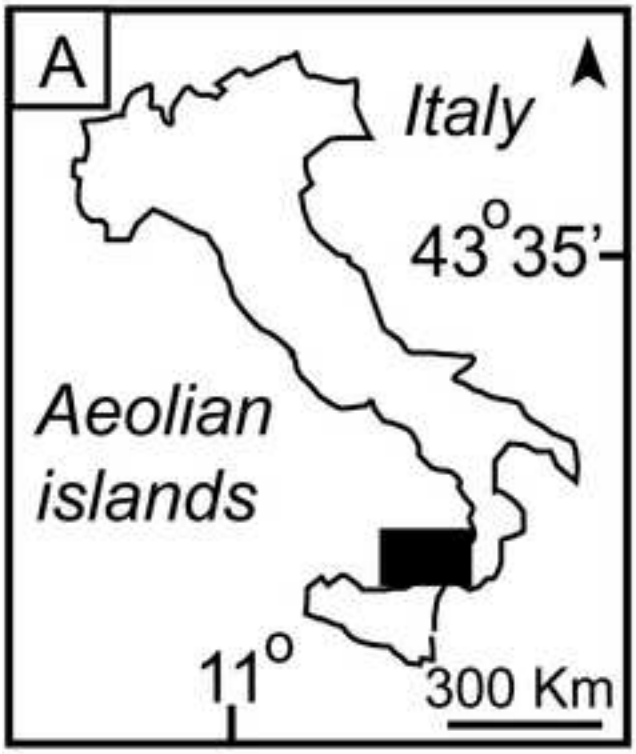

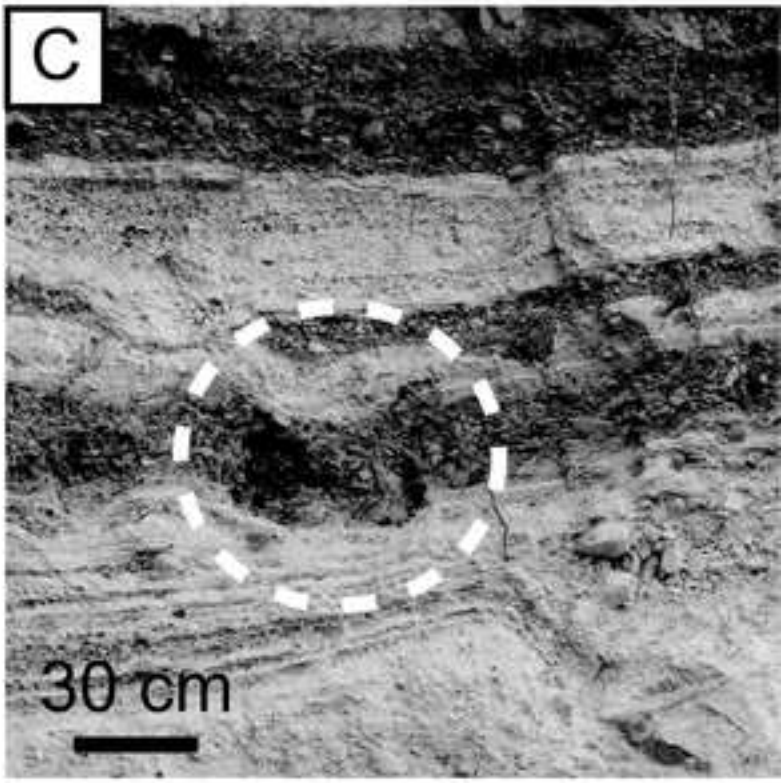

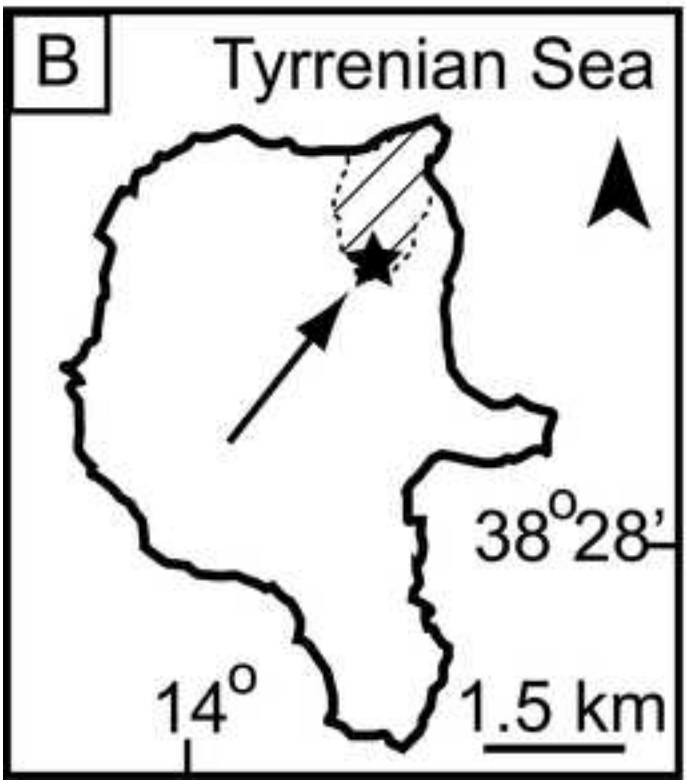

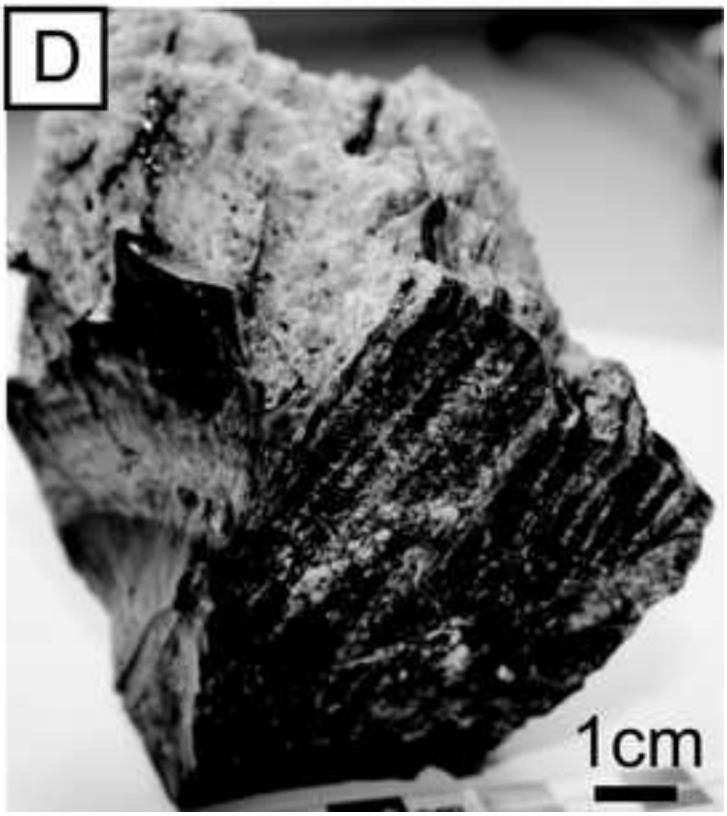

Cabrera Agustin, Figure 2. jpg

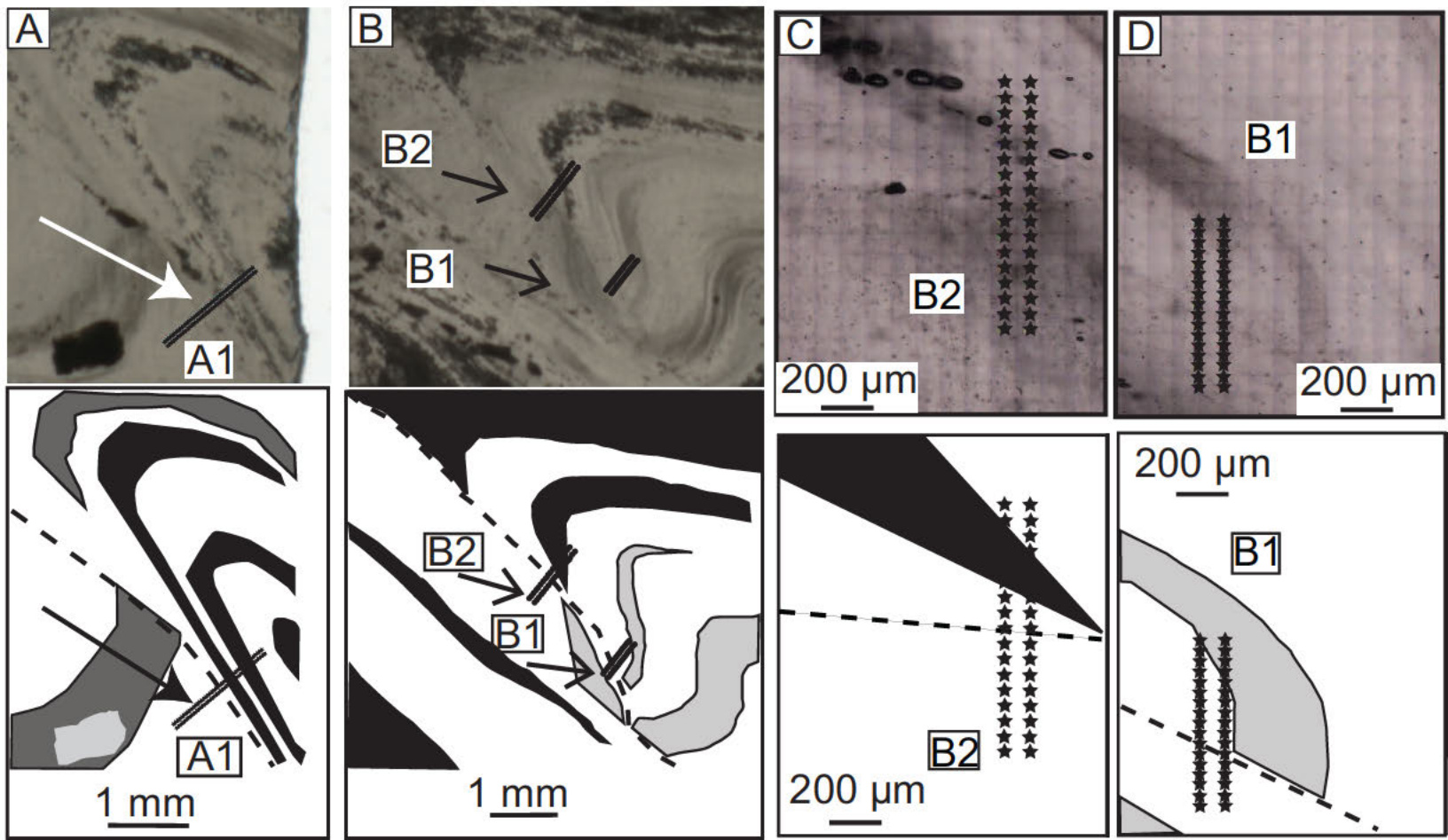

Cabrera Agustin, Figure 2. jpg

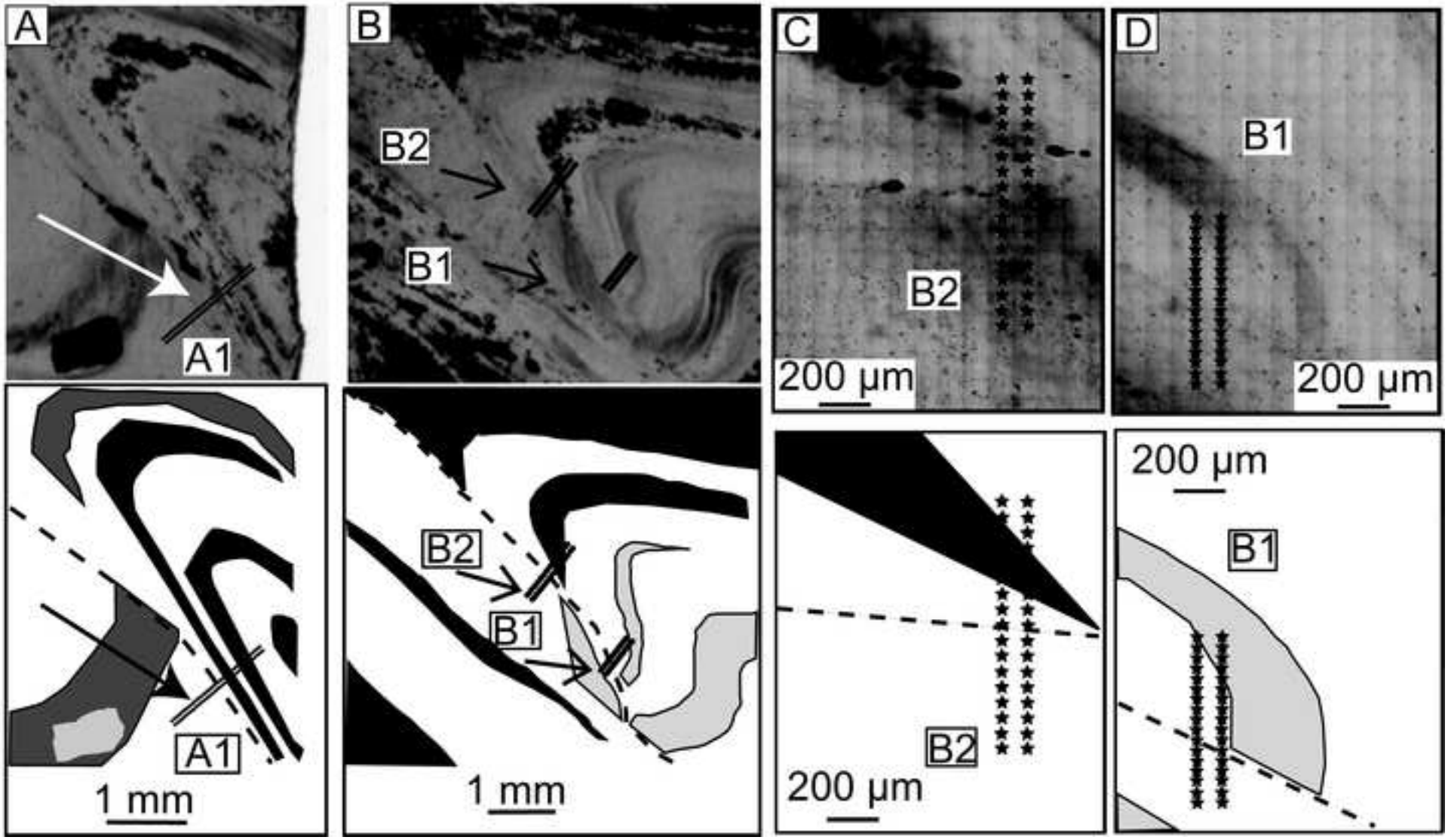

Cabrera Agustin, Figure 3.jpg

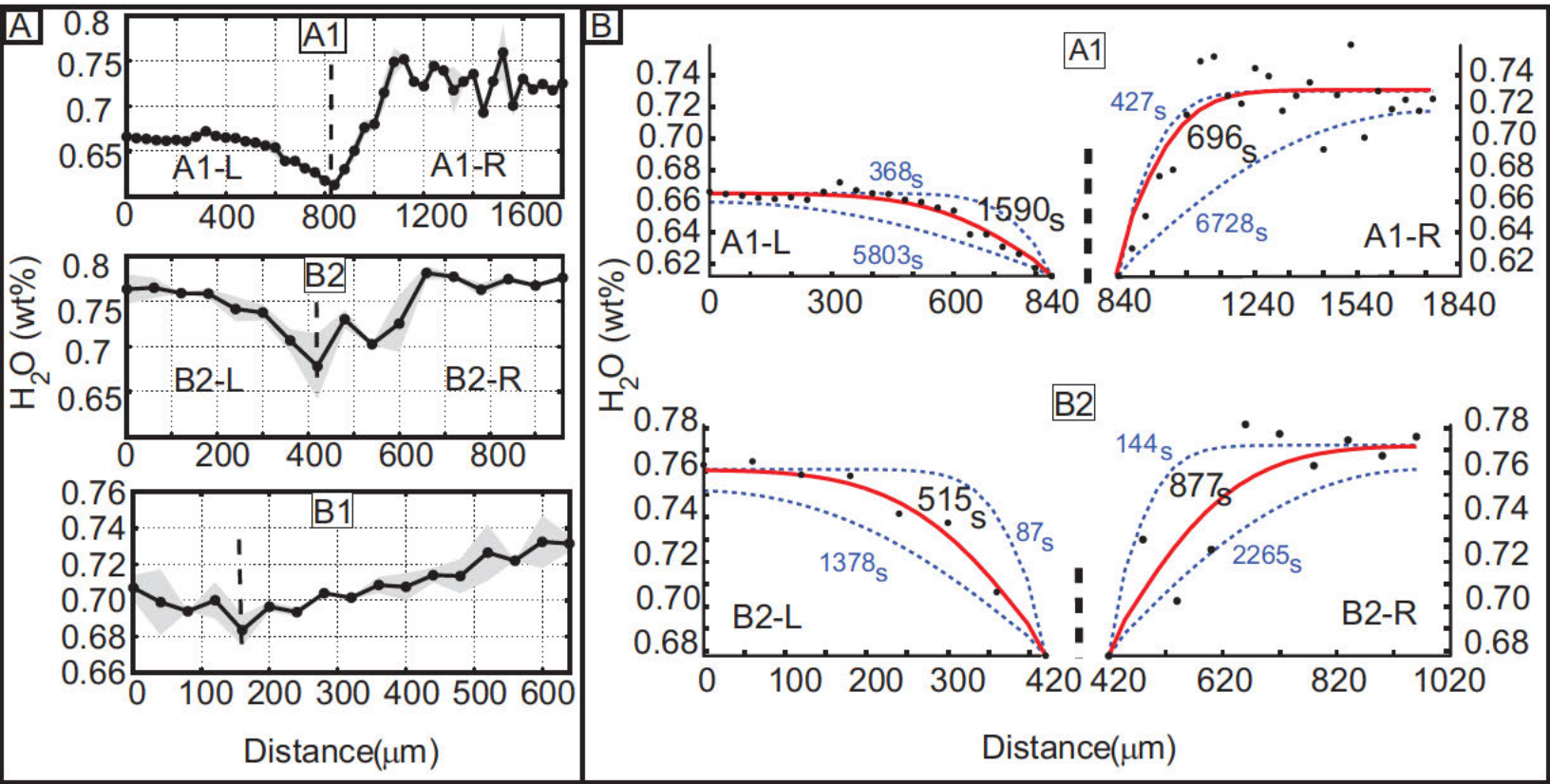

Cabrera Agustin, Figure 3.jpg

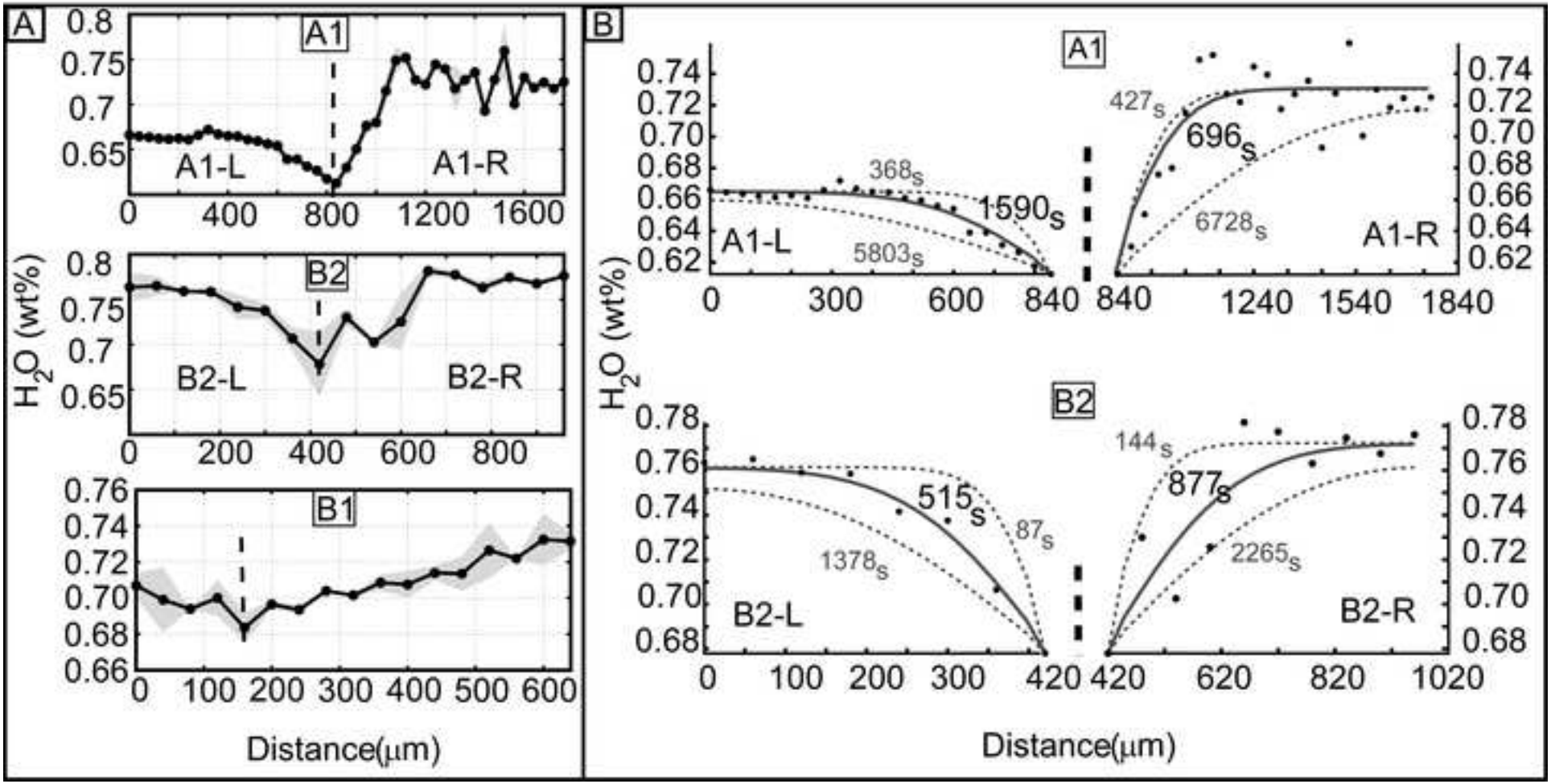

Cabrera Agustin, Figure 4.jpg

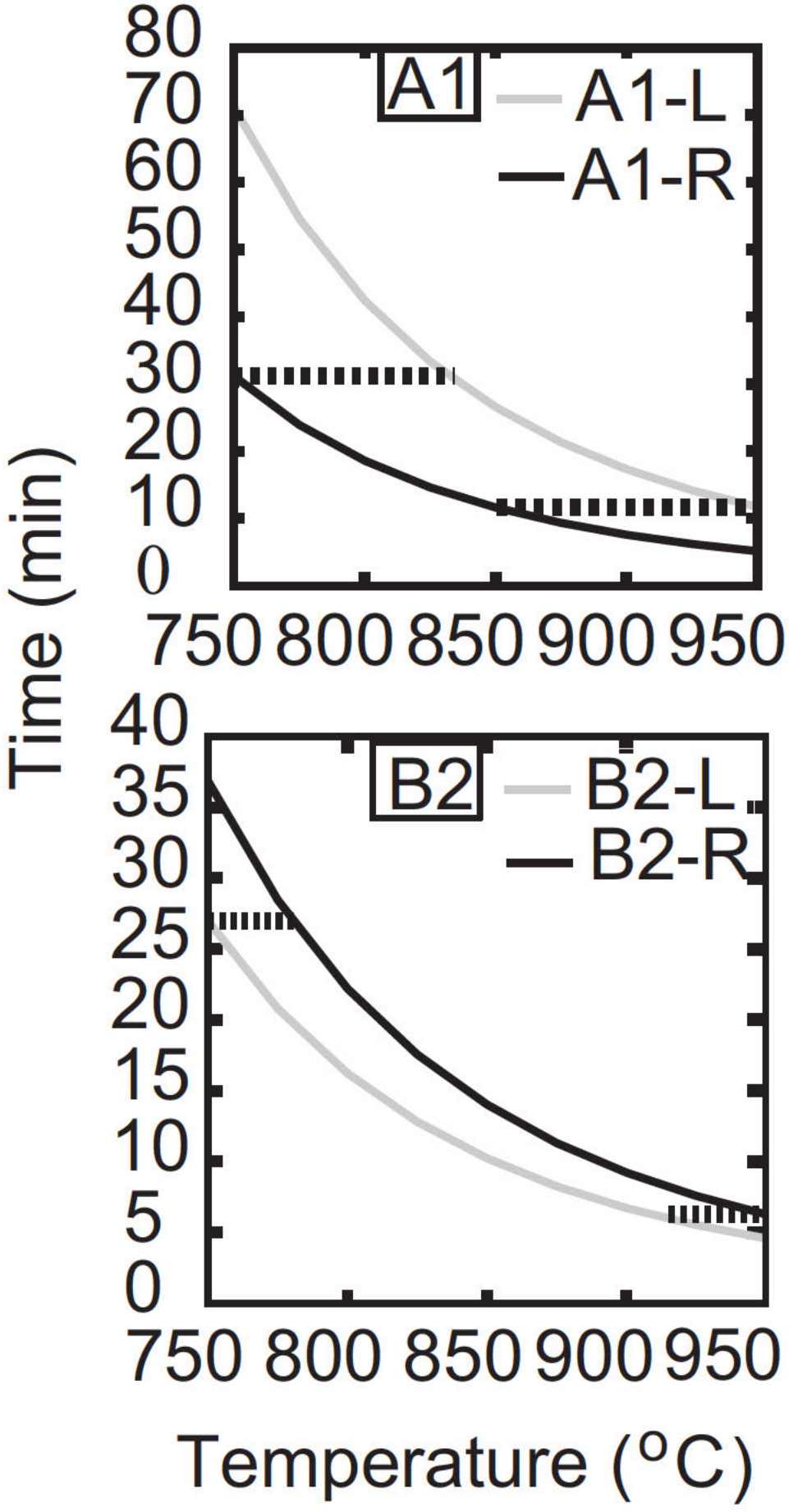

Cabrera Agustin, Figure 4.jpg